Volume 17
Number 44
28 November 2021
Pages 9989–10162

Soft Matter

rsc.li/soft-matter-journal

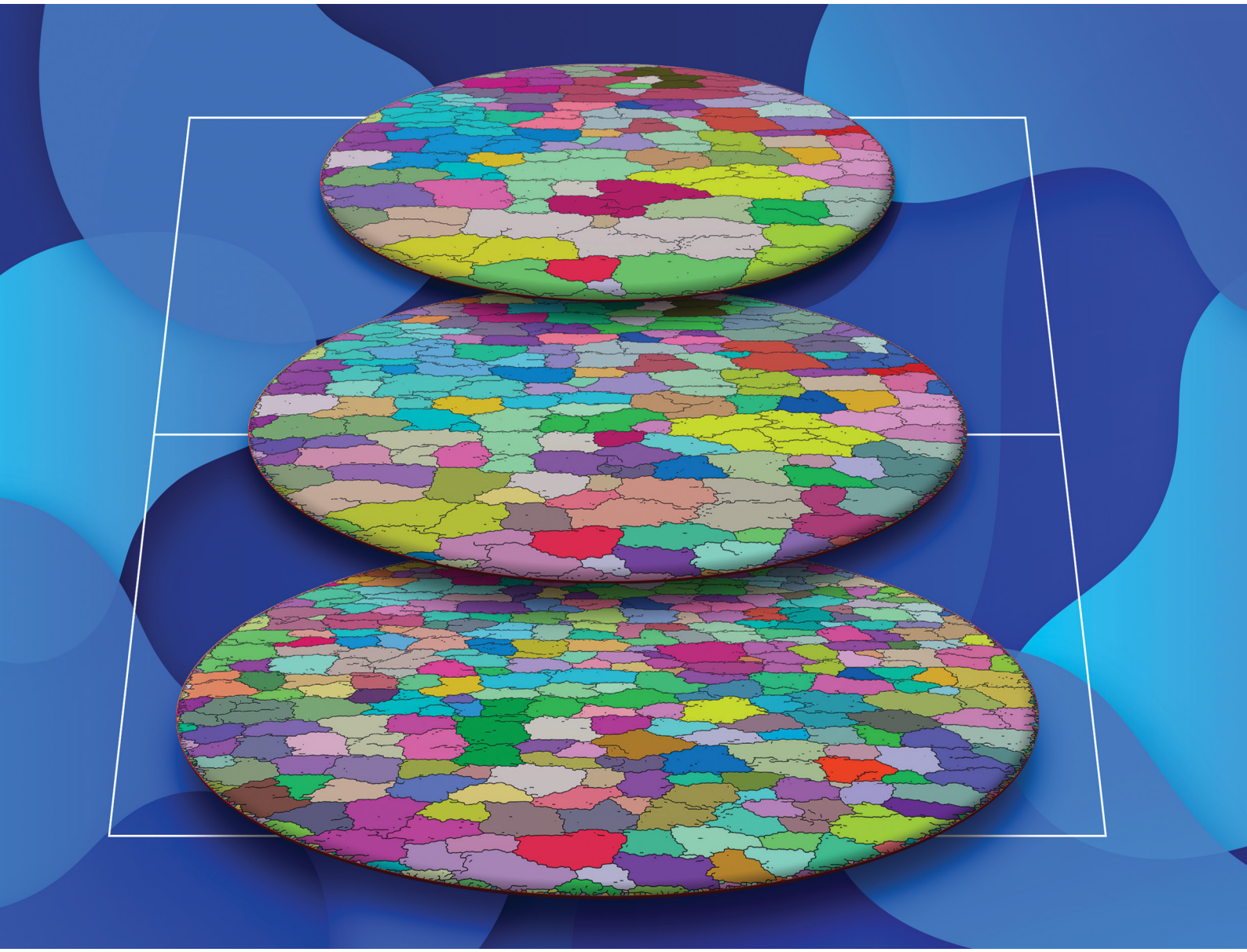

ISSN 1744-6848

ROYAL SOCIETY OF CHEMISTRY

PAPER
Ferenc Kun *et al.*
Evolution of anisotropic crack patterns in shrinking material layers

Soft Matter

PAPER

Cite this: *Soft Matter*, 2021, **17**, 10005

Evolution of anisotropic crack patterns in shrinking material layers

Roland Szatmári, [a] Zoltán Halász, [ab] Akio Nakahara, [c] So Kitsunezaki [d] and Ferenc Kun *[a]

Received 15th August 2021,
Accepted 21st September 2021

DOI: 10.1039/d1sm01193f

rsc.li/soft-matter-journal

Anisotropic crack patterns emerging in desiccating layers of pastes on a substrate can be exploited for controlled cracking with potential applications in microelectronic manufacturing. We investigate such possibilities of crack patterning in the framework of a discrete element model focusing on the temporal and spatial evolution of anisotropic crack patterns as a thin material layer gradually shrinks. In the model a homogeneous material is considered with an inherent structural disorder where anisotropy is captured by the directional dependence of the local cohesive strength. We demonstrate that there exists a threshold anisotropy below which crack initiation and propagation is determined by the disordered micro-structure, giving rise to cellular crack patterns. When the strength of anisotropy is sufficiently high, cracking is found to evolve through three distinct phases of aligned cracking which slices the sample, secondary cracking in the perpendicular direction, and finally binary fragmentation following the formation of a connected crack network. The anisotropic crack pattern results in fragments with a shape anisotropy which gradually gets reduced as binary fragmentation proceeds. The statistics of fragment masses exhibits a high degree of robustness described by a log-normal functional form at all anisotropies.

1 Introduction

Shrinkage induced cracking of thin material layers attached to a substrate is abundant in nature giving rise to the formation of spectacular polygonal crack patterns. Examples can be mentioned on a wide range of length scales from dried lake beds through permafrost regions on Earth and Mars, to the three-dimensional structures of columnar joints formed in cooling volcanic lava.[1,2] The simplest realization of such crack patterns can be achieved in the laboratory by desiccating thin layers of dense suspensions such as coffee,[3] clay,[4–6] or calcium carbonate[7] on a rigid substrate where the gradual solidification leads to shrinkage stresses and cracking. A very important characteristic feature of the emerging crack patterns is the cellular structure which has a high degree of isotropy in the crack orientation.[1,3–11]

Controlled cracking of thin material layers, including the guidance of cracks along predefined paths and the structuring of crack patterns, has a great technological potential especially for microelectronic manufacturing.[12–14] Recently, a promising method of the generation of controlled crack patterns has been suggested by applying mechanical excitation to dense suspensions before desiccation sets in. It has been demonstrated experimentally for calcium carbonate and magnesium carbonate hydroxide pastes that subjecting the paste to vibration or flow the emerging desiccation crack pattern remembers the direction of excitation.[7,15] Detailed investigations have revealed that the mechanical excitation imprints a directional or spatial distribution of density fluctuations and plastic deformation in the paste which affects the local mechanical strength of the solidifying material and in turn shows up in the crack structure.[16–18] Varying the way of excitation, furthermore, the strength and range of interaction of colloidal particles it was demonstrated that the memory effect of pastes provides an efficient way of controlled generation of crack patterns in thin layers.[19,20]

In a homogeneous paste the position and orientation of cracks are determined by the local stress field induced by shrinkage and by the disorder of the material. The cellular crack patterns obtained in unperturbed pastes with an isotropic orientation of cracks is a fingerprint of the dominance of materials' disorder in crack initiation.[3–7,10] The density fluctuation and plastic deformation imprinted by the initial mechanical excitation overcome the effect of disorder and give rise to

[a] *Department of Theoretical Physics, Doctoral School of Physics, Faculty of Science and Technology, University of Debrecen, P.O. Box 400, Debrecen, H-4002, Hungary. E-mail: ferenc.kun@science.unideb.hu; Web: https://mikkamakka.phys.unideb.hu/~feri/*
[b] *Institute for Nuclear Research (Atomki), P.O. Box 51, Debrecen, H-4001, Hungary*
[c] *Laboratory of Physics, College of Science and Technology, Nihon University, 7-24-1 Narashinodai, Funabashi, 274-8501, Japan*
[d] *Research Group of Physics, Division of Natural Sciences, Faculty of Nara Women's University, Nara, 630-8506, Japan*

an anisotropic crack structure, where the primary cracks are aligned along a direction determined by the excitation.[19,21] Due to its potential technological applications, here we investigate how the competition of the initially imposed anisotropy and the structural disorder of the thin layer affects the formation of cracks and the overall structure of the crack pattern. We use a discrete element model of a thin material layer attached to a rigid substrate. In the model, structural disorder is introduced through the discretization of the layer on a random lattice of convex polygons which ensures a high degree of isotropy of the mechanical features. The initial anisotropy, generated *e.g.* by shaking in experiments, is captured by introducing orientational dependence for the strength of cohesive elements between a weak and a strong direction. Varying the strength of anisotropy at a fixed degree of disorder we show that the competition of the two leads to a highly complex behavior. In particular, above a threshold anisotropy shrinkage induced cracking evolves through three distinct phases: (I) formation of primary cracks aligned with the strong direction, (II) secondary cracking in the perpendicular direction, and (III) binary breakup of fragments after a connected fracture network is established. Based on computer simulations we give a detailed quantitative characterization of the three phases. The shape of fragments of the layer proved to be sensitive to the initial anisotropy, however, we demonstrate that the mass (size) distribution of fragments has a high degree of robustness characterized by a log-normal functional form at all anisotropies.

2 Discrete element model of a shrinking layer on a substrate

Recently, we have introduced a discrete element model (DEM) of a thin brittle layer attached to a rigid substrate, which captures the essential mechanisms of the deformation and fracture induced by gradual shrinking.[22] In the following we briefly summarize the main components of the model construction highlighting how the anisotropic characteristics of the layer are implemented.

2.1 Geometry and discretization

In order to reduce directional effects imposed by the sample boundary, we considered a circular layer of radius R, which is also a typical experimental setup used in laboratory measurements.[15] The layer is discretized in terms of randomly shaped convex polygons which are created by a regularized Voronoi tessellation of a rectangle.[23,24] The model system was obtained by cutting out a circular sample from the polygonal random lattice which has a high degree of structural isotropy. The polygons represent material elements which have three degrees of freedom in two dimensions, *i.e.* the two coordinates (x_i, y_i) of the center of mass, and the rotation angle ϕ_i $(i = 1,\ldots,N)$. Here N denotes the total number of polygons of the sample.

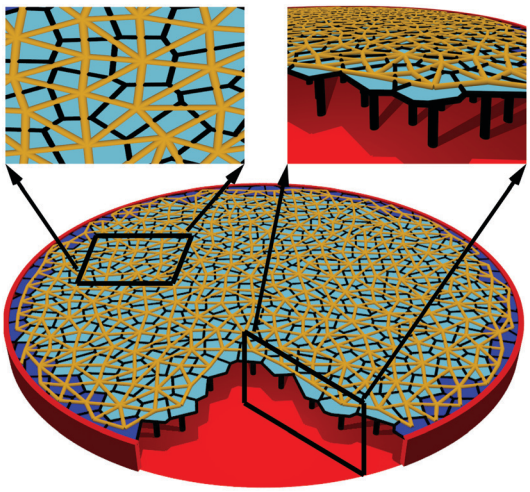

Fig. 1 Main components of the model construction: the shrinking layer is discretized in terms of convex polygons. The circular sample was cut out from the Voronoi tessellation of a rectangle. The polygons and beams (yellow lines) in between represent material elements and their cohesive breakable contacts, respectively. The beam elements form a triangular lattice attached to polygons. The adhesion of the layer is captured by springs coupling the center of polygons to the underlying plane. The boundary polygons of the sample, highlighted by blue color, are fixed to the container wall (red cylinder around the sample).

In order to capture the mechanical behavior of the material, the center of mass of polygons, which are nearest neighbors in the initial Voronoi tessellation, are connected by beam elements.[22–24] This way a triangular lattice of beams is attached to the polygonal structure, see Fig. 1 for an illustration of the model construction. The geometrical properties of beams depend on the random tessellation such that the initial length l_0^{ij} and cross section S_0^{ij} of beams are the distance of the centers and of the length of the common side of the connected polygons i and j, respectively.[22] During the deformation of the system the beams suffer longitudinal deformation, shear, and bending giving rise to forces and torques acting on the polygons. Parameters of the beams as the longitudinal and bending moduli, Poisson ratio, are set such that the model, together with the randomness of the Voronoi lattice, can reproduce the elastic response and mechanical behavior of brittle materials to a good precision under various types of loading conditions.[23,24]

2.2 Adhesion and shrinking

In order to represent the adhesion of the layer to the substrate material, the center of mass of the polygons are coupled to the underlaying plane by spring elements. The springs are stress free in the initial position of the polygons $\vec{r}_i^0 = (x_i^0, y_i^0)$, $(i = 1,\ldots,N)$, however, they exert a restoring force $\vec{F}_i^s$ when the polygons get displaced

$$\vec{F}_i^s = -D_s(\vec{r}_i - \vec{r}_i^0). \quad (1)$$

Here D_s denotes the spring constant characterizing the strength of coupling to the substrate. For simplicity, the same value of D_s is used for all polygons without the possibility to break.

We assume that the thin layer undergoes isotropic shrinking *e.g.* due to desiccation while it is attached to the substrate and to the container wall represented by the boundary polygons (see Fig. 1). To capture the effect of shrinking, in the model the natural length of beams l^{ij} is gradually decreased as a function of time t

$$l^{ij} = l_0^{ij}(1 - st), \tag{2}$$

where s denotes the constant shrinking rate. This time evolution gives rise to a uniform shrinkage strain

$$\varepsilon = (l_0^{ij} - l^{ij})/l_0^{ij} = st, \tag{3}$$

which increases linearly with time. Since the coupling to the substrate and to the side walls prevents the free relaxation, stresses build up in the material. To mimic the effect of the container wall, along the external boundary of the sample the particles are fixed, *i.e.* no displacement and rotation of boundary polygons are allowed.

2.3 Breaking of cohesive bonds

In order to represent the shrinkage induced breakup of the layer, in the model we assume that solely the beams connecting the particles can break, while the spring elements between the particles and the substrate are not breakable. The local stretching and shear (bending) contributes to the breaking of a beam according to a physical breaking rule

$$\left(\frac{\varepsilon_{ij}^{\mathrm{b}}}{\varepsilon_{\mathrm{th}}}\right)^2 + \frac{\max(|\Theta^i|, |\Theta^j|)}{\Theta_{\mathrm{th}}} \geq 1, \tag{4}$$

where the first and second terms capture the contributions of stretching and bending at the beam ends, respectively.[2,23] Here $\varepsilon_{ij}^{\mathrm{b}}$ denotes the longitudinal strain of the beam between particles i and j, while Θ^i, and Θ^j are the bending angles at the beam ends.[22] The breaking criterion eqn (4) is evaluated at each iteration step and those beams which fulfill the condition are removed from the simulations. The subsequent removal of beams leads to the formation of cracks in the layer. Note that the fixed boundary condition, *i.e.* the coupling to the container wall can give rise to a slight shearing of the beams in spite of the isotropic shrinking.

The value of the breaking parameters $\varepsilon_{\mathrm{th}}$ and Θ_{th} control the relative importance of the stretching and bending modes of breaking. We assume that the plastic deformation imprinted by the initial mechanical excitation in pastes introduces a directional dependence of the fracture strength of the solidifying paste. In order to capture this effect in the model, the breaking thresholds $\varepsilon_{\mathrm{th}}$ and Θ_{th} do not have any randomness, however, we assume that they depend on the orientation angle α of the beam with respect to the x axis, which represents *e.g.* the direction of shaking in the initial configuration. For simplicity, we implemented the functional forms

$$\begin{aligned} \varepsilon_{\mathrm{th}}(\alpha) &= \varepsilon_{\mathrm{th}}^0(1 + a\cos\alpha), \\ \Theta_{\mathrm{th}}(\alpha) &= \Theta_{\mathrm{th}}^0(1 + a\cos\alpha), \end{aligned} \tag{5}$$

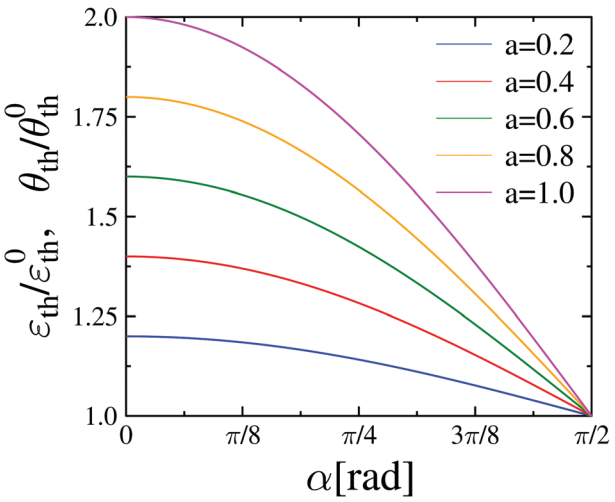

Fig. 2 Angular dependence of the breaking parameters $\varepsilon_{\mathrm{th}}$ and Θ_{th}. The angle α is measured from the x axis of the coordinate system demonstrated in Fig. 3.

where the orientation angle α takes values in the range $0 \leq \alpha \leq \pi/2$ (Fig. 2). In spite of the homogeneity of the structural and mechanical properties, the angular dependence eqn (5) gives rise to an anisotropy of the fracture characteristics of the layer. The strength of anisotropy is controlled by the parameter a, which can be varied from 0 (isotropy) to large values $a \gg 1$ realizing the limit of highly anisotropic behavior. The parameters $\varepsilon_{\mathrm{th}}^0$ and Θ_{th}^0 set the scale of beam strength such that at a given value of the anisotropy a the thresholds $\varepsilon_{\mathrm{th}}$ and Θ_{th} vary from $\varepsilon_{\mathrm{th}}^0$ to $(1 + a)\varepsilon_{\mathrm{th}}^0$, and from Θ_{th}^0 to $(1 + a)\Theta_{\mathrm{th}}^0$, respectively.

When two polygons i and j, which are not coupled by beams (because *e.g.* the beam connecting them is broken), come into contact during the breakup process, an elastic restoring force F_{ij}^{c} is introduced between them. This contact force is assumed to be proportional to the overlap area A_{ij} of contacting polygons and to the Young modulus Y of the material.[22] Since the loading condition ensures the opening of cracks, the contact force has solely a minor role in the simulations.

Discrete element simulations were performed by solving the equation of motion of the polygonal particles by means of a 5th order Predictor–Corrector scheme.[25] The motion of particles was strongly damped by a velocity dependent friction force. The shrinking rate was set to a low value so that the damping force was sufficient to suppress oscillations. For each parameter set averages were calculated over 40 simulations with different realizations of disorder of the Voronoi lattice. The values of the main parameters of the model are summarized in Table 1.

3 Breaking mechanism at different anisotropies

We performed a large amount of computer simulations varying the value of a in the range $0 \leq a \leq 5$ to reveal how the anisotropy affects the evolution of the fracture process and the structure of the emerging crack network as the layer gradually

Table 1 Parameter values used in the simulations

Parameter		Value
System radius	R	60 cm
Average number of polygons	N	11 500
Average number of beams	N_B	33 700
Typical size of a single element		1.0 cm
Density	ρ	5 g cm^{-3}
Elements Young modulus	Y	1×10^{10} dyn cm^{-2}
Beams Young modulus	E	5×10^{9} dyn cm^{-2}
Spring constant	D_s	6×10^{8} dyn cm^{-1}
Time step	δt	3×10^{-7} s
Shrinking rate	s	5×10^{-3} s^{-1}
Minimum strength	ε_{th}^{0}	0.015
Minimum strength	Θ_{th}^{0}	3.0°

shrinks. To quantify the overall damage suffered by the layer during the fracture process, we introduced the fraction of broken beams $d(t)$ with the definition $d(t) = N_b(t)/N_B$, where N_b and N_B denote the number of beams broken up to time t and the total number of beams in the layer in the initial state, respectively. It is a very important feature of our model that it contains solely a single source of disorder, *i.e.* the discretization of the material on a random lattice of convex polygons which introduces structural disorder without any directional dependence. Hence, for zero anisotropy $a = 0$ of the breaking thresholds, representing the absence of initial mechanical excitation in experiments, a cellular crack pattern is expected with a high degree of isotropy of the crack orientation. This is illustrated in Fig. 3 where snapshots of the evolution of the crack pattern are shown at $a = 0$ for 4 different values of the damage parameter d. Before beam breaking starts, shrinking of the layer results in a homogeneous stress field, so that cracks nucleate at random locations. In agreement with former studies,[1,22,26] during their growth cracks can undergo crack tip splitting and branching as it can be observed in Fig. 3(a). As shrinking proceeds, the growing cracks merge and gradually form a connected fracture network along which the layer falls apart into fragments. This point is reached somewhere between Fig. 3(c and d) at about the damage $d_c \approx 0.28$. Further shrinking results in crack formation typically in the middle of the fragments which breaks them into two pieces gradually reducing their size (Fig. 3(c and d)).

Simulations revealed that the presence of anisotropy $a > 0$ has a strong effect both on the initiation and propagation of cracks, which in turn shows up also in the structure of the crack pattern and in the geometrical features of fragments. This is demonstrated by Fig. 4 for the case of $a = 1$ presenting 4 snapshots of the evolution at different stages d of the fracture process. Due to the directional dependence of the local strength ε_{th} and Θ_{th}, in the initial phase of the fracture process those beams break which have a higher angle $\alpha \approx \pi/2$ with the horizontal direction. Removal of beams create micro-cracks along the edges of polygons, which are nearly perpendicular to the beam direction. As a consequence, the primary cracks grow mainly along the horizontal direction as it can be observed in Fig. 4(a). As the strain increases in the layer with

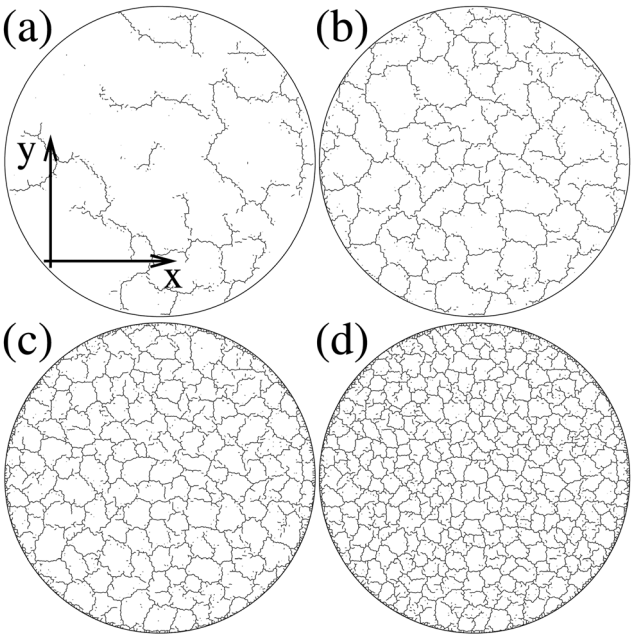

Fig. 3 Time evolution of cracking in an isotropic layer $a = 0$. Snapshots are presented at different values of the fraction of broken fibers d: (a) 0.06, (b) 0.14, (c) 0.22, (d) 0.30. Cracks nucleate at random positions and gradually grow (a and b). Fragments are formed when the entire crack network becomes connected, which occurs between (c) and (d). Further shrinking gives rise to binary break up of the fragments (d), which gradually reduce their size. Note the cellular structure of the crack network with a high degree of isotropy of the crack orientation. (a) Also demonstrates the coordinate system which is used throughout the presentation of the results.

shrinking, stronger beams at a lower angle with the horizontal direction start also to break creating cracks even along the vertical direction in Fig. 4(b). When the fully connected crack network appears, the strong alignment of cracks results in a pronounced anisotropy of the emerging fragments (Fig. 4(c)). It is interesting to note that as shrinking proceeds, in agreement with former experimental and theoretical studies,[1,26–28] the largest deformation occurs around the middle of fragments which favors crack formation perpendicular to the longest extension of fragments. This mechanism results in splitting the fragments into two pieces of nearly equal size gradually reducing the anisotropy of fragments (Fig. 4(d)). These qualitative observations will be quantitatively explored in the next sections.

4 Three phases of cracking

Before beam breaking sets on, a homogeneous stress field builds up in the layer so that the first crack nucleates at a beam which has a high strain and a low breaking threshold. The structural disorder has the consequence that those beams which are longer and thinner suffer a larger local deformation and start breaking at the earliest if they have a large angle $\alpha \approx \pi/2$ with the horizontal direction. To characterize how crack initiation is affected by the presence of anisotropy,

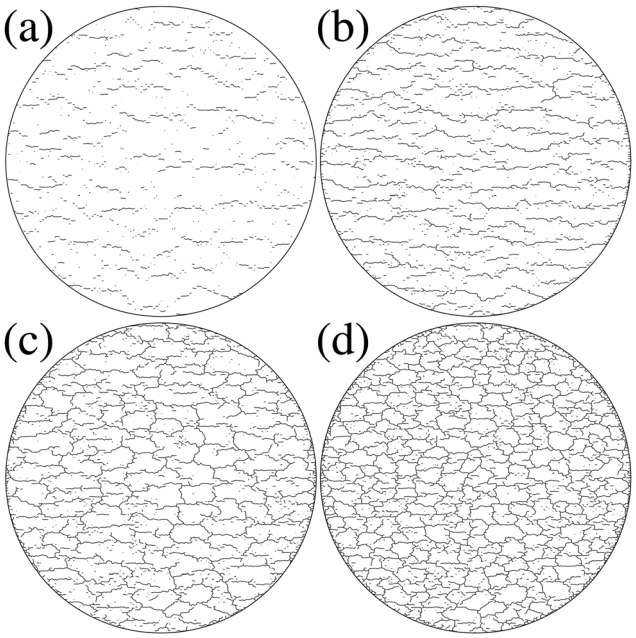

Fig. 4 Time evolution of the cracking thin layer in the presence of anisotropy $a = 1$. Snapshots are presented at different values of the fraction of broken fibers d: (a) 0.06, (b) 0.14, (c) 0.22, (d) 0.30. Primary cracks are aligned with the horizontal direction (a and b). The connected crack network emerges when secondary cracks vertically connect the primary ones (c). Initially, fragments have a strong anisotropy (c), which is then gradually reduced by binary breakup (d).

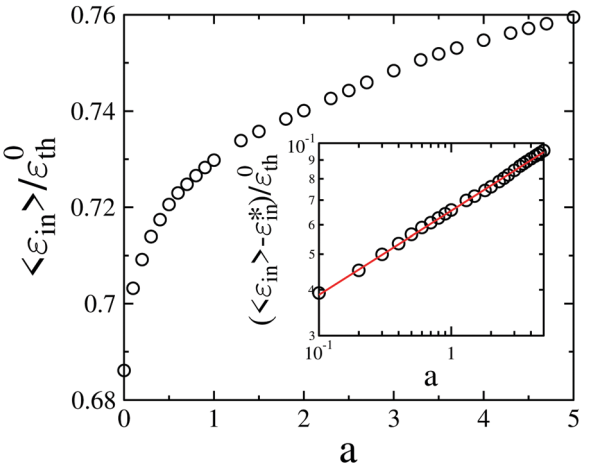

Fig. 5 The average value of the shrinkage strain $\langle\varepsilon_{in}\rangle$ where the first crack nucleate in the layer scaled with the breaking parameter ε_{th}^0 as a function of the degree of anisotropy. The inset demonstrates that subtracting an appropriate constant ε_{in}^* from the curve of the main panel a power law dependence is obtained on a.

we determined the average value $\langle\varepsilon_{in}\rangle$ of the shrinkage strain ε_{in} where the first micro-crack nucleates in the system. It can be observed in Fig. 5 that the crack initiation strain $\langle\varepsilon_{in}\rangle$ steeply increases already at the smallest anisotropies $0 \lesssim a$ and it has a monotonous behavior over the entire range of the parameter a considered. To quantify how the deviation of $\langle\varepsilon_{in}\rangle$ from the isotropic case $\langle\varepsilon_{in}\rangle$ ($a = 0$) increases with growing anisotropy, in the inset of Fig. 5 we replotted the difference of $\langle\varepsilon_{in}\rangle - \varepsilon_{in}^*$ as a function of a. Of course, the value of the constant ε_{in}^* should fall close to $\langle\varepsilon_{in}\rangle(a = 0)$, however, we tunned it as a free parameter to obtain the best straight line on a double logarithmic plot. The good quality straight line observed in the inset of Fig. 5 confirms that the crack initiation strain has a power law dependence on the degree of anisotropy

$$\langle\varepsilon_{in}\rangle = \varepsilon_{in}^* + Ba^{\beta}. \quad (6)$$

The value of the exponent β was obtained by fitting $\beta = 0.22 \pm 0.01$, while the additive constant is $\varepsilon_{in}^*/\varepsilon_{th}^0 = 0.664$. We can get an estimate of the value of $\langle\varepsilon_{in}\rangle$ by assuming that all the beams have the same deformation and no polygons suffer rotation up to the time when the first micro-crack occurs. In this case that beam should break first which has the highest angle α_{max} with the horizontal. Averaging α_{max} over the samples, the value $\langle\alpha_{max}\rangle$ we obtain is close but not equal to $\pi/2$. Taylor expanding the cosine around $\pi/2$, from eqn (5) we can obtain an approximate expression of the crack initiation strain $\langle\varepsilon_{in}\rangle \approx \varepsilon_{th}^0(1 + a(\pi/2 - \langle\alpha_{max}\rangle))$, which is consistent with eqn (6), however, the strength of anisotropy a has a higher exponent $\beta = 1$. The lower value of β obtained by computer simulations is due to the fluctuations of the local deformation caused by the inherent structural disorder of the sample.

4.1 Angular distribution of macro-cracks

When a beam breaks, a micro-crack is formed along the common edge of the two polygons. As shrinking proceeds additional micro-cracks nucleate and gradually grow by the breaking of adjacent beams resulting in extended macro-cracks. To obtain a clear view on the structure of the evolving crack pattern, we worked out an algorithm which constructs the macro-cracks of the layer starting from individual micro-cracks. A macro-crack is identified as a continuous path of polygon edges with broken beams spanning between two junction points. A junction point of the crack network is a polygon corner from which either one, or three micro-cracks start. Polygon corners where two micro-cracks meet are considered to be internal points of macro-cracks, while junctions of one and three micro-cracks are end points of arrested cracks, and the merging points of independent cracks, respectively. The algorithm starts by identifying the junction points of one and three micro-cracks. Then considering a junction point as the start of a macro-crack, the algorithm follows the crack path until another junction point is reached defining the other end of the macro-crack. The algorithm is demonstrated in Fig. 6. Due to the randomness of the polygonal lattice, the crack path is never straight, instead it has a zig-zag structure. Macro-cracks are characterized by their length l and orientation, which are determined as the sum of the length of polygon edges along the crack path, and as the angle Θ between the x axis and the straight line connecting the two end junctions of the crack. In the evolving system, cracks are always identified in snapshots which has the consequence that the merging of a younger crack

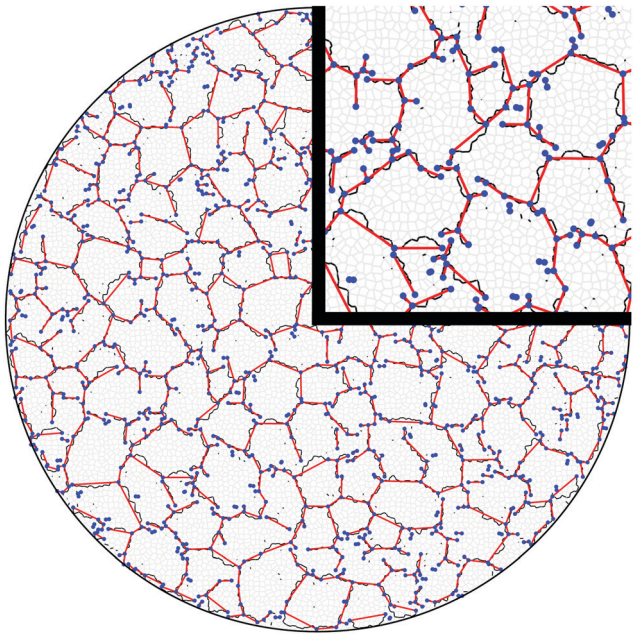

Fig. 6 Identification of junction points (blue dots) and macro-crack in a snapshot of the damaged layer for the isotropic case $a = 0$. For clarity, the underlying polygonal structure is also presented, however, macro-cracks composed of a single polygon edge are removed. The straight lines connect the two end junctions of macro-cracks. In the upper right corner a magnified view on a smaller area is shown.

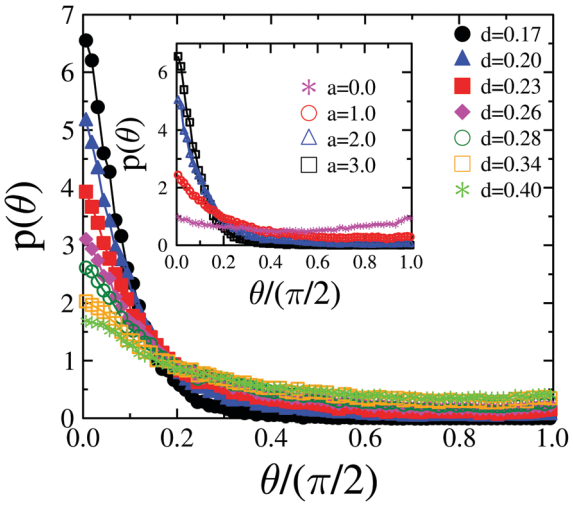

Fig. 7 Probability distribution $p(\Theta)$ of the orientation angle Θ of macro-cracks at the anisotropy $a = 3$ for several values of the damage fraction d. For small d the distribution is strongly peaked at $\Theta \approx 0$, however, as fracture proceeds the curves are gradually flattening. Inset: The distribution $p(\Theta)$ for several degrees of anisotropy a obtained at the same damage fraction $d = 0.17$. Note that as a increases the peak at $\Theta \approx 0$ gets gradually more pronounced.

with an older one results in the reduction of crack length by creating a new junction point in the crack interior.

The probability distribution $p(\Theta)$ of the orientation angle Θ is presented in Fig. 7 for an anisotropic system $a = 3$ at several values of the damage fraction d. It can be observed that at early stages of the fracture process the distribution is strongly peaked around $\Theta \approx 0$, which shows that the primary cracks are strongly aligned with the horizontal direction. As breaking proceeds, cracks also develop at higher angles Θ so that the alignment gets gradually less pronounced quantified by the flattening of the distribution $p(\Theta)$. Angular distributions obtained at different degrees of anisotropy a are compared in the inset of Fig. 7 at the same value of the damage fraction $d = 0.17$ at an early stage of breakup. The strong effect of anisotropy on the crack orientation is evident, *i.e.* the distribution is nearly uniform for the case of isotropy $a = 0$, however, increasing a suppresses cracks at large angles, *e.g.* in case of $a = 3$ there are no cracks with $\Theta > 0.3$ in the layer at this d value.

4.2 Transition from primary to secondary cracking

The results imply that primary cracks, nucleated at the beginning of the fracture process are strongly aligned with the horizontal direction (*i.e.* the strong direction). However, due to the complex deformation field emerging in the damaged layer, later nucleating secondary cracks tend to have a higher angle with the primary ones. To understand how this transition of the dominant orientation occurs, first we determined the number of cracks $N_{\parallel}$ and $N_{\perp}$, having an orientation angle below and above $\pi/4$ with the horizontal direction, respectively, in consecutive snapshots of the system with a fixed difference of damage $\Delta d = 2.8 \times 10^{-3}$. Then the increments $n_{\perp} = N_{\perp}(d + \Delta d) - N_{\perp}(d)$ and $n_{\parallel} = N_{\parallel}(d + \Delta d) - N_{\parallel}(d)$ of the crack numbers were obtained. Fig. 8 presents both quantities $n_{\perp}$, and $n_{\parallel}$ as function of damage d. It can be observed that for the isotropic case $a = 0$ the curves of $n_{\perp}(d)$ and $n_{\parallel}(d)$ practically coincide over the entire d range considered, which shows the absence of any preferred direction of crack formation. However, anisotropy $a > 0$ results in a clear separation of the increments $n_{\perp} \ll n_{\parallel}$ for low damages, *i.e.* at the beginning of the fracture process the nucleation and growth of cracks parallel to the horizontal direction dominate indicated by the increasing rate $n_{\parallel}$, whereas hardly any cracks are created at large angles with the horizontal $n_{\perp} \approx 0$. With increasing damage d the increment $n_{\parallel}$ passes a maximum and attains a local minimum practically at the same d where cracking in the perpendicular direction sets on with an increasing $n_{\perp}$. As the anisotropy a increases this feature of the cracking mechanism gets more pronounced in such a way, that for $a > 0.4$ a finite damage fraction has to be reached to get the first crack at an angle $\Theta > \pi/4$ with the horizontal. In this range of anisotropy two distinct phases of cracking can be distinguished separated by a characteristic damage fraction d_{ps}: at low damage $d < d_{ps}$ the phase of primary cracking is characterized by $n_{\perp} \approx 0$ and $n_{\parallel} > 0$ implying the strong alignment of cracks along the horizontal direction, while at $d > d_{ps}$ in the phase of secondary cracking $n_{\perp} \approx n_{\parallel}$ holds, and both increments are growing with d. Simulations revealed that the stronger the anisotropy is, the sharper the transition becomes shifting also the threshold value d_{ps} towards higher damages. This can also be clearly observed in the snapshots presented in Fig. 4 for the case of $a = 1$.

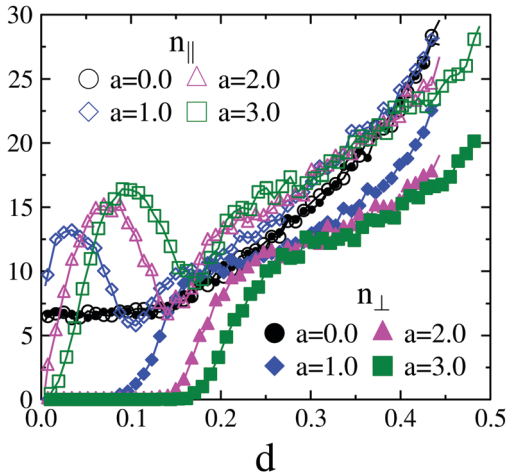

Fig. 8 Increments of the number of cracks of different directions as function of the damage fraction d at several anisotropies. The corresponding curves of $n_{\parallel}$ and $n_{\perp}$ are represented by the open and filled symbols, respectively.

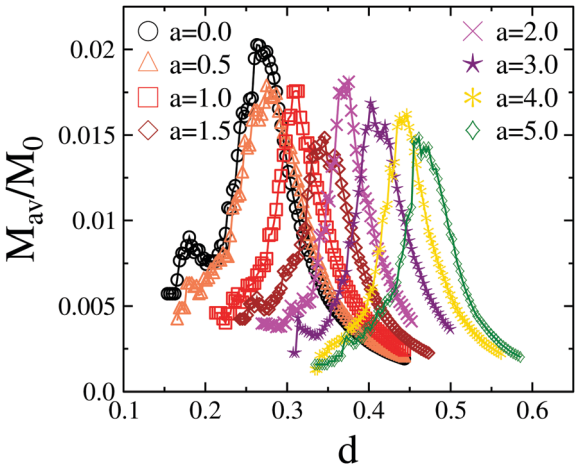

Fig. 9 Average mass of fragments M_{av} obtained from eqn (8) as a function of the damage fraction d for several values of the anisotropy parameter a. M_{av} is scaled with the total mass M_0 of the system. The position of the maximum $d_c(a)$ marks the point of the dynamics where the evolving crack network becomes globally connected. The stronger alignment of primary cracks at higher anisotropies has the consequence that the position of the maximum shifts to higher values with increasing a.

4.3 Connected crack network

It is important to note that the primary cracks break the shrinking layer into long thin slices which are then segmented in the perpendicular direction by the secondary cracks. Beyond the transition point d_{ps} from primary to secondary cracking, the evolving crack network has a second critical point where the behavior of the system undergoes qualitative changes. Namely, the damage fraction d_c where the merging of primary and secondary cracks leads to the emergence of a connected crack network along which the layer falls apart into a large number of fragments. This critical point can be determined by studying the evolution of fragments, which are defined as sets of polygons connected by the surviving intact beams at a given shrinkage strain. Since fragments are enclosed by cracks, they first occur in the layer in a large amount at the critical point d_c. Before the emergence of the spanning crack network the layer is damaged, however, it practically keeps its integrity. In order to characterize how the transition from the damaged to the fragmented state occurs during the desiccation process, we determined the average mass of fragments M_{av} as a function of damage d. After identifying the fragments, for a single sample the average fragment mass was calculated as the ratio of the second M_2 and first M_1 moments of fragment masses m_i, $i = 1,\ldots,K$, where K denotes the total number of fragments in the layer at a given d. The qth moment of the fragment ensemble is defined as

$$M_q = \sum_{i=1}^{K}{}' m_i^q, \tag{7}$$

where the $'$ indicates that the largest fragment mass M_{max} is skipped in the summation. Then M_{av} was obtained by averaging the value of M_2/M_1 over 40 samples at each anisotropy

$$M_{av} = \langle M_2/M_1 \rangle. \tag{8}$$

It can be observed in Fig. 9 that the $M_{av}(d)$ curves have a well defined maximum the position of which d_c depends on the degree of anisotropy a. Fragment formation starts in the secondary cracking regime $d > d_{ps}$ due to the merging of cracks of widely different orientation angles. For higher anisotropy a the segmentation sets on at a higher damage d_{ps}, which has the consequence that fragment formation requires also a higher fraction of broken beams. However, these early fragments are much smaller than the original size of the system. Since the largest fragment is always omitted in the calculation of moments M_q, the position of the maximum d_c marks the point where the crack network gets connected and spans the entire system so that the dominating fragment suddenly breaks up into a large number of pieces.[29,30] Beyond the maximum no dominating fragment exists, and all fragments undergo gradual breakup as shrinking proceeds. It follows that depending on the value of damage d the regime of secondary cracking $d > d_{ps}$ can be sub-divided into damaged and fragmented phases with a transition point at d_c, where the crack network gets connected. Of course, the critical damage fraction d_c monotonically increases with the anisotropy.

4.4 Phase diagram of the system

Based on the analysis of the crack orientation and of the overall structure of the emerging crack network we conclude that the evolution of the crack pattern of shrinkage induced fracturing of a thin layer has essentially three phases: (I) primary cracking is dominated by the formation of long cracks aligned with a direction imprinted by the initial mechanical excitation. (II) Secondary cracking sets on when cracks even perpendicular to the primary ones are generated. As shrinking proceeds, primary and secondary cracks merge which leads to the emergence of a connected network of cracks spanning the entire system (phase (III)).

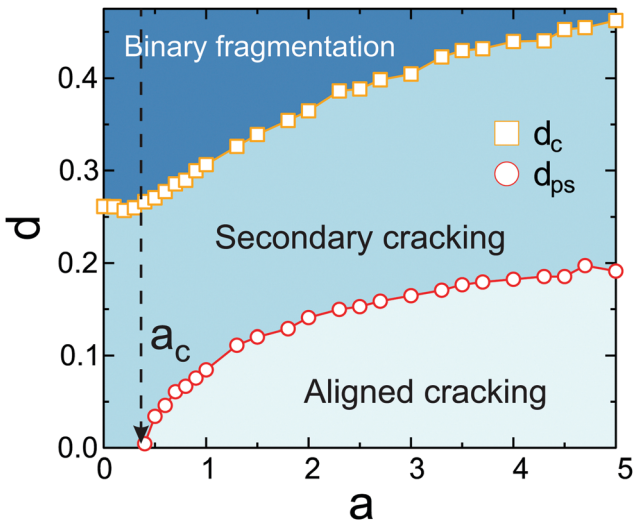

Fig. 10 The three phases of shrinkage induced cracking on the damage-anisotropy parameter plane. The vertical dashed line indicates that at low anisotropies $a < a_c$ only weak alignment of cracks occur so that cracks of any direction may form already at low damage. Above the threshold anisotropy $a > a_c$, the beginning of the fracture process is dominated by aligned cracking, so that secondary cracks segmenting the sliced sample start to occur above the phase boundary d_{ps}. As the damage d further increases, the merging of cracks leads to the emergence of a connected crack network at d_c and binary fragmentation sets on.

Based on computer simulations, we determined the transition points d_{ps} and d_c for a large number of anisotropies a and constructed the phase diagram of the system on the damage-anisotropy parameter plane, which is illustrated in Fig. 10. Simulations revealed that at low anisotropies, only weak alignment of crack occurs so that already at low damages cracks of any orientation may be generated in the system. Beyond the threshold anisotropy $a_c \approx 0.4$ indicated by the vertical dashed line in Fig. 10, strongly aligned cracks dominate the beginning of shrinkage induced cracking $d < d_{ps}$ slicing the sample. The damage has to surpass the threshold value d_{ps} to obtain secondary cracks segmenting the long slices in the perpendicular direction. The dynamics of breakup changes at the damage d_c, where the connected crack network emerges and binary fragmentation sets on. It can be observed in the phase diagram that both threshold damages d_{sp} and d_c are increasing with the anisotropy a. Note that below the threshold anisotropy $a < a_c$ the cracking process has only two phases, *i.e.* the primary and secondary regimes cannot be separated. This is caused by the structural disorder of the sample, which favors random isotropic orientation of cracks. The value of a has to surpass the threshold anisotropy a_c to overcome the effect of disorder.

5 Binary fragmentation

The emergence of the connected crack network which spans the entire system has the consequence that the layer breaks up into a large number of fragments. As shrinking proceeds, the fragments accumulate strain again which results in crack formation typically starting from the middle of the fragment (see also Fig. 3 and 4). As a consequence, fragments undergo a sequence of binary breakup events gradually reducing their mass (size).

5.1 Evolution of the shape of fragments

The structure of the crack network strongly depends on the degree of anisotropy, hence, it can be expected that anisotropy affects also the evolution of the fragmentation process. The long straight cracks of primary cracking create elongated slices in the layer, which are then segmented by the secondary cracks into smaller pieces. This mechanism results in fragments whose elongated shape originates from the structure of the connected crack network formed at the critical damage fraction d_c. To characterize the shape of fragments we determined the bounding box of individual pieces with side length L_x and L_y directed along the x and y axis of the initial coordinate system, respectively. For illustration see the inset of Fig. 12. As a shape descriptor the dimensionless ratio L_y/L_x was averaged over the ensemble of fragments at a given damage fraction d.[31,32]

It can be observed in Fig. 11 that in the absence of initial anisotropy $a = 0$, fragments have an isotropic shape $\langle L_y/L_x \rangle \approx 1$ at any damage state d during the evolution of the system. However, anisotropy $a > 0$ of the local materials' strength gives rise to an elongated fragment shape $\langle L_y/L_x \rangle < 1$ such that the higher a is, the more elongated the fragments get. It is interesting to note that the degree of shape anisotropy is the highest (*i.e.* $\langle L_y/L_x \rangle$ is the smallest) at the fragmentation critical point d_c, where the majority of fragments are first created. During the binary fragmentation process, cracks have a higher probability to divide the longer side of fragments into two pieces, which gradually increases the aspect

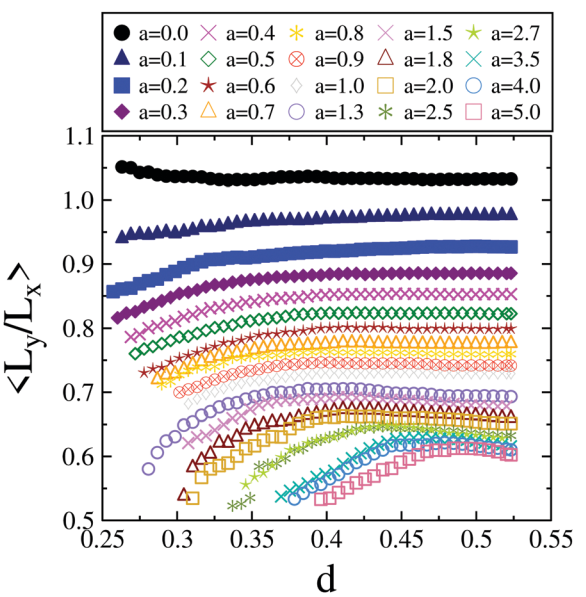

Fig. 11 The average aspect ratio $\langle L_y/L_x \rangle$ of fragments as a function of the damage fraction d for several anisotropies a. Note that the asymptotic value r_{yx} of the aspect ratio decreases with a and it attains a limit value at $r_{yx} \approx 0.62$.

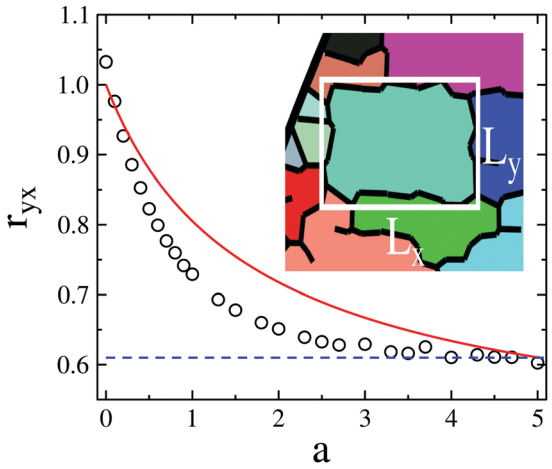

Fig. 12 Asymptotic value r_{yx} of the aspect ratio $\langle L_y/L_x \rangle$ as a function of the anisotropy parameter a. The dashed straight line represents the limit value $r_{yx} \approx 0.62$, which characterizes the stable shape of fragments. The continuous red line is the analytic approximation of r_{yx} obtained from eqn (9) with the parameter value $\mu = 0.64$. The inset presents a magnified view on a small region of the sample, where fragments are highlighted by different colors. The construction of the bounding box with side lengths L_x and L_y is illustrated for a fragment.

ratio (*i.e.* reduces the shape anisotropy). Simulations revealed that in all cases of initial anisotropy $a > 0$ the binary fragmentation gradually reduces the size of fragments but at the same time it leads to the emergence of a stable fragment shape characterized by the asymptotic value of the aspect ratio $\langle L_y/L_x \rangle \to r_{yx}$. It can be seen in Fig. 12 that the asymptotic aspect ratio r_{yx} decreases with increasing initial anisotropy a but attains a limit value $r_{yx} \approx 0.62$.

In the final state the average shape of fragments is governed by the minimization of the accumulating elastic energy E_{el}.[1] Assuming that the linear extension of stable fragments falls below the characteristic length of the elastic field, from the minimization of E_{el} we can obtain the asymptotic aspect ratio r_{yx} as a function of the strength of anisotropy a

$$r_{yx} \approx \sqrt{\frac{2 + a(1-\mu)}{2 + a(1+\mu)}}, \qquad (9)$$

where the parameter μ is related to the Poissonian number ν of the layer as $\nu = (1-\mu)/(1+\mu)$. Fig. 12 shows that this analytical expression provides a reasonable approximation of the numerical results with $\mu = 0.64$. Eqn (9) implies that for very large anisotropies $a \to \infty$ the stable aspect ratio r_{yx} tends to the limit $r_{yx} \to \sqrt{(1-\mu)/(1+\mu)} = \sqrt{\nu}$. Substituting the limit value $r_{yx} = 0.62$ yields $\nu \approx 0.38$, which is somewhat higher than the Poissonian number of the layer obtained from simulations $\nu \approx 0.2$.

5.2 Mass distribution of fragments

Computer simulations revealed that in spite of the complexity of the evolution of fragment shapes, the statistics of their mass exhibits a high degree of robustness. Fig. 13 presents the mass distribution $p(m, d)$ of fragments obtained at several different

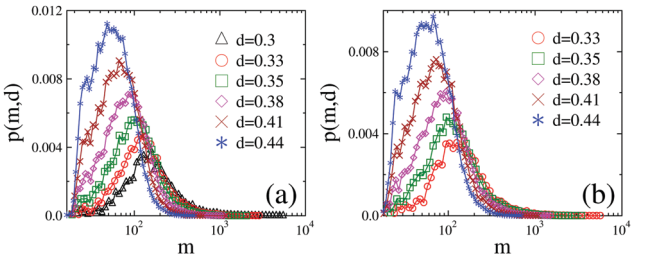

Fig. 13 Mass distributions at different damage fractions d for two values of the anisotropy parameter $a = 0$ (a) and $a = 1$ (b). As d increases the functional form of the curves remains practically the same, only the average size of the fragments gets reduced.

damage fractions above the fragmentation critical point $d > d_c$ for two values of the anisotropy parameter $a = 0$ and $a = 1$. Using logarithmic scale on the horizontal axis, the distributions are nearly symmetric for both anisotropies at all shrinkage stages d, however, with increasing d both the average mass of fragments $\langle m \rangle$ and the upper cutoff m_{max} of the distributions are decreasing. Note that around the lower cutoff m_{min} of the fragment mass, the shape of the distributions gets somewhat distorted, which becomes more pronounced for higher damages d. This behavior is caused by the existence of unbreakable polygons, which does not allow small fragments to further reduce their size, and hence, modifies the statistics in the low mass range.

Fig. 14 demonstrates that rescaling the mass distributions with the average mass of fragments $\langle m \rangle$ the $p(m, d)$ curves of different d can be collapsed on a master curve. The high quality data collapse implies the scaling structure of the distributions

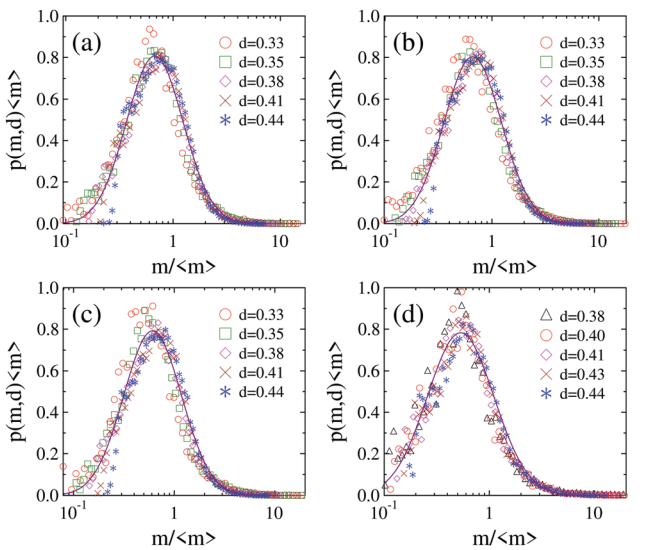

Fig. 14 Scaling plot of the mass distributions $p(m, d)$ of fragments at four different anisotropies a: (a) $a = 0$, (b) $a = 0.5$, (c) $a = 1$, (d) $a = 2$. Rescaling the distributions with the average fragment mass $\langle m \rangle$, the curves obtained at different damages $d > d_c$ can be collapsed on the top of each other. The continuous lines represent fits with the log-normal distribution eqn (11).

$$p(m, d) = \langle m \rangle^{-1} \Psi(m/\langle m \rangle), \quad (10)$$

where d dependence on the right hand side only occurs through the average of fragment masses $\langle m \rangle(d)$. It is important to emphasize that the scaling structure eqn (10) is valid for all anisotropies a. This result again shows the robustness of the statistics of fragment masses (sizes) which can be attributed to the generic binary fragmentation mechanism.[22,28,33]

The scaling function $\Psi(x)$ can be very well described by the log-normal distribution

$$\Psi(x) = \frac{1}{x\sigma\sqrt{2\pi}} \exp\left[-(\ln(x) - \mu)^2/2\sigma^2)\right], \quad (11)$$

where μ and σ denote the logarithmic average and the standard deviation, respectively. The continuous lines in Fig. 14 present fits of the numerical data with eqn (11). Deviations from eqn (11) can be observed in the regime of small fragment masses due to the existence of unbreakable fragments (single polygons).

The log-normal mass distribution is consistent with the binary splitting of the fragments which gives rise to a cascade process of fragment creation.[22,28,33–35]

6 Discussion

Crack formation under mechanical load drives the failure of materials, and hence, it is typically undesired in applications. However, recent investigations have revealed that the initiation, propagation, and arrest of cracks can be controlled in thin material layers by imposing local curvature,[14] by patterning the underlying substrate surface,[12] and by mechanical perturbation of dense suspensions before they start drying.[7,15,19] Here we focused on the desiccation induced cracking of a thin layer attached to a substrate in which anisotropy was imprinted by initial vibration or flow. We constructed a discrete element model of a layer of disordered micro-structure where anisotropy was captured by introducing directional dependence for the strength of the cohesive coupling of material elements. Computer simulations were performed varying the strength of anisotropy a in a broad range while other parameters of the model were fixed.

Our study revealed that there exists a threshold anisotropy a_c below which the material's disorder dominates the initiation and growth of cracks resulting in a cellular crack pattern close to the completely isotropic case. When the anisotropy is sufficiently high $a > a_c$, the cracking is found to evolve through three distinct phases: the beginning of the process is dominated by strongly aligned cracks which create slices in the sample. Crack formation in the perpendicular direction sets on above a critical value of the damage d_{ps}, which results in segmentation of the sliced regions. The merging of cracks leads to the emergence of a connected crack network along which the sample falls apart into a large number of pieces. This occurs at a second critical point d_c beyond which further shrinkage results in binary fragmentation breaking the fragments into two pieces. As the anisotropy increases, the critical damages of the transition points d_{ps} and d_c shift to higher values.

We demonstrated that the shape of fragments formed at the critical point d_c inherits the anisotropy of the fracture pattern. Further shrinking generates cracks typically in the middle of the fragments perpendicular to their longer side, which drives the fragment shape towards isotropy. Consequently, the aspect ratio gradually increases with increasing damage but approaches an asymptotic value, which depends on the initial anisotropy a of the system. Simulations revealed that the asymptotic aspect ratio of fragments decreases as the strength of initial anisotropy grows converging to a finite lower bound. It is a very interesting outcome of our study that in spite of the strong effect of anisotropy on the structure of the crack pattern and on the shape of emerging pieces, the size (mass) distribution of fragments exhibits a high degree of robustness. Namely, at any parameter set a log-normal mass distribution was obtained which shows that binary breakup governs the statistics of fragment masses.

Although, we implemented a phenomenological representation of the anisotropy induced by the initial mechanical perturbation of dense pastes, the results of our discrete element simulations are in a good qualitative agreement with the experimental findings of ref. 7, 15, 19, 20, 33 and 35 on the evolution of the crack pattern and on the size (mass) distribution of fragments. Based on the literature, we could make a quantitative comparison to the final state fragment shape obtained in ref. 7. Fig. 7(c) of ref. 7 presents the final state of the desiccation process of a calcium carbonate layer which was initially subject to strong shaking in the vertical direction. In the digital image we determined the aspect ratio of the fragments as 0.614 ± 0.021, which is in a very good agreement with the asymptotic value $r_{yx} = 0.62$ obtained in our simulations. The flexibility of DEM simulations made it possible to unveil the entire phase structure of the system as the degree of anisotropy is gradually changed at a fixed amount of disorder. For a detailed quantitative comparison to the evolution of real desiccation crack patterns further laboratory measurements are needed which are already in progress.

From the viewpoint of application, it is an important feature of our DEM that the anisotropy of the local cohesive strength has a spatial homogeneity which makes the position of the aligned primary cracks random along the perpendicular direction similar to the measurements of ref. 7 and 19. Careful experiments have revealed that inplane mechanical perturbation like shaking allows for the control of the direction of primary cracks while their position still remains stochastic. Position control can be achieved by vertical perturbation in the initial state *e.g.* by imprinting the paste with Faraday waves.[19] Our modelling approach can be further extended to capture the effect of such spatial inhomogeneities of the initial state.

Conflicts of interest

There are no conflicts to declare.

Acknowledgements

This research was supported by the National Research, Development and Innovation Fund of Hungary, financed under the K-16 funding scheme Project No. K 119967. Project No. TKP2020-IKA-04 has been implemented with the support provided from the National Research, Development and Innovation Fund of Hungary, financed under the 2020-4.1.1-TKP2020 funding scheme. This work was supported by JSPS KAKENHI Grant Numbers 18K03560 and 20K03886.

Notes and references

1 L. Goehring, A. Nakahara, T. Dutta, S. Kitsunezaki and S. Tarafdar, *Desiccation Cracks and their Patterns: Formation and Modelling in Science and Nature*, John Wiley & Sons, 2015.
2 *Statistical models for the fracture of disordered media*, ed. H. J. Herrmann and S. Roux, Elsevier, Amsterdam, 1990.
3 A. Groisman and E. Kaplan, *Europhys. Lett.*, 1994, **25**, 415.
4 H. Nahlawi and J. K. Kodikara, *Geotech. Geol. Eng.*, 2006, **24**, 1641–1664.
5 S. Nag, S. Sinha, S. Sadhukhan, T. Dutta and S. Tarafdar, *J. Phys.: Condens. Matter*, 2010, **22**, 015402.
6 L. Goehring, R. Conroy, A. Akhter, W. J. Clegg and A. F. Routh, *Soft Matter*, 2010, **6**, 3562–3567.
7 A. Nakahara and Y. Matsuo, *J. Stat. Mech.: Theor. Exp.*, 2006, P07016.
8 S. Bohn, L. Pauchard and Y. Couder, *Phys. Rev. E: Stat., Nonlinear, Soft Matter Phys.*, 2005, **71**, 046214.
9 W. Wang, A. Li, X. Zhang and Y. Yin, *Phys. A*, 2011, **390**, 2678–2685.
10 V. Lazarus and L. Pauchard, *Soft Matter*, 2011, **7**, 2552–2559.
11 J. C. Flores, *Soft Matter*, 2017, **13**, 1352–1356.
12 K. H. Nam, I. H. Park and S. H. Ko, *Nature*, 2012, **485**, 221–224.
13 L. Guo, Y. Ren, L. Y. Kong, W. K. Chim and S. Y. Chiam, *Nat. Commun.*, 2016, **7**, 13148.
14 N. P. Mitchell, V. Koning, V. Vitelli and W. T. M. Irvine, *Nat. Mater.*, 2017, **16**, 89–93.
15 A. Nakahara and Y. Matsuo, *Phys. Rev. E: Stat., Nonlinear, Soft Matter Phys.*, 2006, **74**, 045102.
16 M. Otsuki, *Phys. Rev. E: Stat., Nonlinear, Soft Matter Phys.*, 2005, **72**, 046115.
17 O. Takeshi, *Phys. Rev. E: Stat., Nonlinear, Soft Matter Phys.*, 2008, **77**, 061501.
18 T. Ooshida, *J. Phys. Soc. Jpn.*, 2009, **78**, 104801.
19 H. Nakayama, Y. Matsuo, O. Takeshi and A. Nakahara, *Eur. Phys. J. E: Soft Matter Biol. Phys.*, 2013, **36**, 1.
20 Y. Matsuo and A. Nakahara, *J. Phys. Soc. Jpn.*, 2012, **81**, 024801.
21 S. Kitsunezaki, A. Nakahara and Y. Matsuo, *Europhys. Lett.*, 2016, **114**, 64002.
22 Z. Halász, A. Nakahara, S. Kitsunezaki and F. Kun, *Phys. Rev. E*, 2017, **96**, 033006.
23 F. Kun and H. J. Herrmann, *Comput. Meth. Appl. Mech. Eng.*, 1996, **138**, 3.
24 G. A. D'Addetta, F. Kun and E. Ramm, *Granular Matter*, 2002, **4**, 77–90.
25 *Computer Simulation of Liquids*, ed. M. P. Allen and D. J. Tildesley, Oxford University Press, Oxford, 1984.
26 S. Kitsunezaki, *Phys. Rev. E: Stat. Phys., Plasmas, Fluids, Relat. Interdiscip. Top.*, 1999, **60**, 6449–6464.
27 T. Hornig, I. M. Sokolov and A. Blumen, *Phys. Rev. E: Stat. Phys., Plasmas, Fluids, Relat. Interdiscip. Top.*, 1996, **54**, 4293–4298.
28 S. Ito and S. Yukawa, *Phys. Rev. E: Stat., Nonlinear, Soft Matter Phys.*, 2014, **90**, 042909.
29 D. Stauffer and A. Aharony, *Introduction to Percolation Theory*, Taylor & Francis, 1992.
30 F. Kun and H. J. Herrmann, *Phys. Rev. E: Stat. Phys., Plasmas, Fluids, Relat. Interdiscip. Top.*, 1999, **59**, 2623.
31 G. Domokos, F. Kun, A. A. Sipos and T. Szabó, *Sci. Rep.*, 2015, **5**, 9147.
32 G. Domokos, D. J. Jerolmack, F. Kun and J. Török, *Proc. Natl. Acad. Sci. U. S. A.*, 2020, **117**, 18178–18185.
33 S. Ito and S. Yukawa, *J. Phys. Soc. Jpn.*, 2014, **83**, 124005.
34 J. A. Aström, *Adv. Phys.*, 2006, **55**, 247–278.
35 S. Ito, A. Nakahara and S. Yukawa, *Transition properties in dynamical and statistical features of drying crack patterns*, 2020.